

***Ab initio* calculation of electron-impact-ionization cross sections for ions in exotic electron configurations**

John Jasper Bekx,^{1,2,*} Sang-Kil Son,^{1,3} Robin Santra,^{1,2,3} and Beata Ziaja^{1,3,4}

¹*Center for Free-Electron Laser Science, Deutsches Elektronen-Synchrotron DESY, Notkestrasse 85, 22607 Hamburg, Germany*

²*Department of Physics, University of Hamburg, Jungiusstrasse 9, 20355 Hamburg, Germany*

³*The Hamburg Centre for Ultrafast Imaging, Luruper Chaussee 149, 22761 Hamburg, Germany*

⁴*Institute of Nuclear Physics, Polish Academy of Sciences, Radzikowskiego 152, 31-342 Kraków, Poland*



(Received 19 April 2018; revised manuscript received 22 June 2018; published 8 August 2018)

Atomic or molecular assemblies irradiated with intense hard x-ray pulses, such as those emitted from x-ray free-electron lasers (XFELs), are subject to a strong ionization, which also releases electrons from atomic inner shells. The resulting core-hole states relax via various channels, including fluorescence and Auger decay. The latter is the predominant relaxation channel for light elements and typically occurs on a time scale of 1–10 fs. In dense samples, the core-hole ions may already undergo electron-impact ionizations during this time due to the abundance of highly energetic photoelectrons and Auger electrons. In this study we perform an *ab initio* calculation of the electron-impact-ionization cross sections of ions with an arbitrary electronic configuration at zero temperature. This allows us to evaluate and compare impact-ionization cross sections for ions in ground and “exotic” electronic states (e.g., with a few core holes), which may be formed during their interaction with intense x-ray pulses. We show that the impact-ionization cross sections for ions of the same charge, but with varying electronic configurations, may significantly differ. This finding has to be taken into account in any modeling tool treating the relaxation of atoms after high-energy-impact collision, e.g., simulations dedicated for coherent x-ray diffraction imaging of nanocrystals and single biological macromolecules, or laser-created plasma studies. Our computationally efficient *ab initio* calculation scheme can be easily incorporated in such simulation schemes.

DOI: [10.1103/PhysRevA.98.022701](https://doi.org/10.1103/PhysRevA.98.022701)

I. INTRODUCTION

Within the last decade, the advent of x-ray free-electron lasers (XFELs) [1–5] has provided novel insights for the study of x-ray–matter interactions. Applications of this knowledge range over various different scientific fields, including atomic and molecular physics [6–9], astrophysics [10], plasma physics [11], and structural biology [12–16].

In particular, XFELs provide ultrashort and ultraintense pulses of x rays, shaping new avenues in x-ray crystallography [17,18]. Three-dimensional determination of biomolecular structures is vital for studying biological functions of these macromolecules. Molecular structures of biomolecules are reconstructed from x-ray scattering patterns. In order to ensure a sufficiently strong scattering signal, the patterns are typically obtained from coherent diffraction on a crystal formed from the macromolecule. However, growing the high-quality crystals is a difficult and sometimes even an impossible task [19]. Instead, the high fluence from the XFEL can be exploited in order to generate a sufficiently strong scattering signal from nanocrystals [13] and single bioparticles [14]. At the same time, such a high fluence induces a rapidly progressing damage of the sample. In order to overcome this issue, the XFEL pulse duration should be sufficiently short (≤ 10 fs) to outrun the nuclear damage. This scheme is called “diffraction before destruction.” However, currently available XFEL pulses are not short enough

to elude electronic motion and the subsequently induced electronic damage [20]. Therefore, quantitative understanding of the radiation damage mechanisms, as well as their proper treatment and incorporation into simulations, is vital for the accuracy of the structure determination from experimental data [20–25]. Such incorporation of radiation damage into photon-matter interaction studies has been done, e.g., with the molecular dynamics code XMDYN [26,27]. Based on a combination of atomistic calculation and classical molecular dynamics, XMDYN provides microscopic simulations of x-ray-induced dynamics of clusters [28], nanocrystals [24], and solid-density matter [29] in connection with x-ray molecular imaging [30].

While interacting with the imaged sample, hard x rays predominantly excite inner-shell electrons. The resulting core-hole states can decay via various paths, including fluorescence and Auger decay. The latter is the predominant relaxation channel for light elements, and typically takes place within 1–10 fs [25,31] after a photoionizing event. At this timescale, in materials dense enough, the core-hole ions may also undergo electron-impact ionization, due to the abundance of highly energetic photoelectrons and Auger electrons.

The importance of impact ionization in radiation damage has been demonstrated not only in connection with x-ray imaging [20,32], but also for electron diffraction [33,34] and plasma studies [11,35]. This ionization process has been extensively studied over many years [36–39]. The accuracy of theoretical methods used for the determination of the electron-impact-ionization cross sections depends both on the wave-function

*Corresponding author: john.jasper.bekx@desy.de

description used to describe the incoming and outgoing electrons, as well as on the collision theory employed. A concise overview can be found in Refs. [40] and [41]. Semiempirical approaches and simplified formulas are also frequently used to determine electron-impact-ionization cross sections, such as the semiempirical formula by Lotz [42–45] and the binary-encounter-Bethe (BEB) formula [46]. The latter method has also been extended to the relativistic regime [47,48].

Here, we intend to describe electron-impact ionization of an ion with any excited electronic configuration which may occur as the result of its exposure to high-intensity x rays. Such cases are not accounted for accurately in semiempirical formulas due to the lack of experimental data on the electron-impact ionization of excited ions. In this paper, we provide an *ab initio* calculation of the electron-impact-ionization cross sections for such ions at zero temperature. In our framework, the impact electron before and after the scattering process is modeled as a plane wave. The target ion, as well as the ejected electron after the scattering process, is treated within a Hartree-Fock-Slater framework, with free states approximated by a discrete pseudocontinuum. With this approach, it is assumed that the outgoing scattered electron and the ejected electron are distinguishable.

The paper is structured as follows: In Sec. II we extend the electronic structure calculation code, XATOM [25,26,49], in order to implement the doubly differential electron-impact-ionization cross section (DDCS) within this scheme. From the DDCS, singly differential (DCS) and total cross sections (CS) are obtained. In Sec. III we calculate the DDCS for an incoming electron of 1 keV energy interacting with a double core-hole ($1s^{-2}$) carbon (+2) ion, as well as the angle- and energy-resolved DCS for the same system. For the total cross-section studies, we consider various electronic configurations of carbon (+), carbon (+2), and sulfur (+8) ions, including their ground states. The results are compared with the available experimental data and other theory models (Lotz and BEB schemes). The section is concluded with a discussion. Section IV provides a conclusion and an outlook.

II. THEORETICAL AND NUMERICAL FRAMEWORK

We start with a clarification of terminology. While discussing the process of electron-impact ionization, we consider the *incoming electron*, which, after the scattering process, becomes the *outgoing (scattered) electron*, and the *electron ejected* from the system.

Throughout this paper, atomic units are employed, i.e., $m_e = e = \hbar = 4\pi\epsilon_0 = 1$, unless specified otherwise.

A. XATOM toolkit

In order to calculate electron-impact-ionization cross sections, we build our implementation on the preexisting XATOM toolkit [25,26,49]. This toolkit treats x-ray-atom interactions in an *ab initio* framework, employing nonrelativistic quantum electrodynamics and perturbation theory. XATOM is capable of calculating rates and cross sections of x-ray-induced processes, including photoionization, Auger decay, x-ray fluorescence, elastic x-ray scattering, and Compton scattering [50,51]. It incorporates a Hartree-Fock-Slater (HFS) description of the

many-electron system, which is an independent-particle approximation with a mean-field Hamiltonian:

$$\hat{H}_{\text{HFS}} = -\frac{1}{2}\nabla^2 - \frac{Z}{|\mathbf{x}|} + \int d^3x' \frac{n(\mathbf{x}')}{|\mathbf{x} - \mathbf{x}'|} + V_{\text{exc}}(\mathbf{x}), \quad (1)$$

where the exchange potential $V_{\text{exc}}(\mathbf{x})$ at zero temperature is of the form [52]

$$V_{\text{exc}}(\mathbf{x}) = -\frac{3}{2} \left[\frac{3}{\pi} n(\mathbf{x}) \right]^{1/3}, \quad (2)$$

and $n(\mathbf{x}) = \sum_i^{\text{occ}} \varphi_i^\dagger(\mathbf{x})\varphi_i(\mathbf{x})$ is the electron density, with $\varphi_i(\mathbf{x})$ denoting a single-particle spin-orbital wave function. Furthermore, the Latter tail correction is applied to this potential to ensure proper fall-off asymptotics [53]. Finally, the central-field approximation is made, imposing spherical symmetry. This enables us to write the solution of the Schrödinger equation in the form

$$\varphi_{nlms}(\mathbf{x}) = \frac{u_{nl}(r)}{r} Y_{lm}(\Omega_{\mathbf{x}}) \begin{pmatrix} \delta_{s,+1/2} \\ \delta_{s,-1/2} \end{pmatrix}, \quad (3)$$

with n , l , m , and s the principal, azimuthal, magnetic, and spin quantum number of the electron with the associated wave function $\varphi_{nlms}(\mathbf{x})$, respectively. Using this ansatz, XATOM subsequently solves the Schrödinger equation in a self-consistent way.

XATOM calculations involve numerous computational input parameters. In particular, the radial coordinate r in Eq. (3) is defined with the generalized pseudospectral method on a nonuniform grid [54], with the number of radial grid points N , the maximum radius R_{max} , and the mapping parameter L , which determines the density distribution of radial grid points [54]. The larger L becomes, the more radial grid points are pushed towards higher values of r . There is also a cutoff parameter imposed on the azimuthal quantum number l , called l_{max} . We used $N = 200$, $L = 10$ a.u., $R_{\text{max}} = 80$ a.u., and $l_{\text{max}} = 35$ for all computations, unless specified otherwise.

B. Doubly differential electron-impact-ionization cross section

The expression for the doubly differential cross section (DDCS) for the inelastic scattering of an electron with a many-electron system is derived in Ref. [55]. The derivation is performed using the Born approximation, which assumes that both the incoming electron and the outgoing scattered electron have a high enough energy to be described by a plane wave. It takes on the form

$$\begin{aligned} \frac{d^2\sigma}{d\Omega_{\mathbf{q}_{\text{out}}} dE_{\text{out}}} &= \frac{4}{Q^4} \frac{q_{\text{out}}}{q_{\text{in}}} \sum_{I,F} P_I \left| \int d^3x \langle F | \hat{n}(\mathbf{x}) | I \rangle e^{i\mathbf{Q}\cdot\mathbf{x}} \right|^2 \\ &\times \delta(E_I - E_F + \omega) \\ &= \frac{4}{Q^4} \frac{q_{\text{out}}}{q_{\text{in}}} \sum_{I,F} P_I |\langle F | \hat{n}^\dagger(\mathbf{Q}) | I \rangle|^2 \delta(E_I - E_F + \omega), \end{aligned} \quad (4)$$

where $\hat{n}(\mathbf{x}) = \hat{\psi}^\dagger(\mathbf{x})\hat{\psi}(\mathbf{x})$ is the electron density operator, with $\hat{\psi}(\mathbf{x})$ being a fermionic field operator. The initial and final momenta of the incoming electron are denoted by \mathbf{q}_{in} and \mathbf{q}_{out} , \mathbf{Q} is their respective difference, $\mathbf{Q} = \mathbf{q}_{\text{in}} - \mathbf{q}_{\text{out}}$, $q_{\text{in}} = |\mathbf{q}_{\text{in}}|$,

$q_{\text{out}} = |\mathbf{q}_{\text{out}}|$, and $Q = |\mathbf{Q}|$. The energies of the incoming and scattered electron are denoted as E_{in} and E_{out} , respectively. $|I\rangle$ and $|F\rangle$ represent the initial and final wave functions of the target system under consideration, and E_I and E_F denote their respective energies. Furthermore, P_I refers to the probability of finding the system in state $|I\rangle$ before the scattering. Finally, ω denotes the energy transfer $E_{\text{in}} - E_{\text{out}}$ from the incoming electron. The $1/Q^4$ dependence is a consequence of the Coulomb interaction between the projectile and the target, and exhibits an angular dependence, $Q^4 = [q_{\text{in}}^2 + q_{\text{out}}^2 - 2q_{\text{in}}q_{\text{out}}\cos(\theta)]^2$, where θ denotes the angle between the direction of the incoming and scattered electron. Azimuthal symmetry is always assumed.

In order to implement Eq. (4) into the HFS framework of XATOM, we introduce a complete orthonormal basis set of spin orbitals $|\varphi_p\rangle$ of the target, with orbital energy ε_p and associated fermionic creation and annihilation operators \hat{c}_p^\dagger and \hat{c}_p , respectively. The index p contains both spatial and spin quantum numbers. The field operator is expanded in this basis as $\hat{\psi}(\mathbf{x}) = \sum_p \varphi_p(\mathbf{x}) \hat{c}_p$. Within an independent-electron model, we approximate our initial state $|I\rangle$ as a single Fock state composed of the aforementioned spin orbitals:

$$|I\rangle \approx |\{N_{el}\}\rangle \equiv \prod_{p=1}^{N_{el}} \hat{c}_p^\dagger |0\rangle, \quad (5)$$

where N_{el} denotes the number of electrons present in the initial state, and $|0\rangle$ is the vacuum state. Furthermore, we neglect all correlations between an electron eventually ejected during the collision and the electrons yet present in the parent ion. Within this approximation, we can write our final state as

$$|F\rangle \approx \hat{c}_f^\dagger \hat{c}_i |\{N_{el}\}\rangle. \quad (6)$$

After invoking these relations, we use the Condon rules [31], which allow for matrix elements with respect to Fock states to be reduced to matrix elements with respect to the spin orbitals. This enables us to transform Eq. (4) into the following form:

$$\begin{aligned} \frac{d^2\sigma}{d\Omega_{\mathbf{q}_{\text{out}}} dE_{\text{out}}} &= \frac{4}{Q^4} \frac{q_{\text{out}}}{q_{\text{in}}} \sum_{\{N_{el}\}} P_{\{N_{el}\}} \sum_{i,f} n_i^{\{N_{el}\}} (1 - n_f^{\{N_{el}\}}) \\ &\times |\langle \varphi_f | e^{i\mathbf{Q}\cdot\mathbf{x}} | \varphi_i \rangle|^2 \delta(\varepsilon_i - \varepsilon_f + \omega) \\ &= \frac{4}{Q^4} \frac{q_{\text{out}}}{q_{\text{in}}} \sum_{i,f} \bar{n}_i (1 - \bar{n}_f) \\ &\times \left| \int d^3x \varphi_f^\dagger(\mathbf{x}) e^{i\mathbf{Q}\cdot\mathbf{x}} \varphi_i(\mathbf{x}) \right|^2 \delta(\varepsilon_i - \varepsilon_f + \omega), \end{aligned} \quad (7)$$

where $n_i^{\{N_{el}\}}$ is the eigenvalue of the number operator $\hat{n}_i = \hat{c}_i^\dagger \hat{c}_i$, which is equal to 0 or 1 due to its fermionic nature. The superscript refers to the state on which the operator is acting on (in this case $|\{N_{el}\}\rangle$). The matrix element is calculated with respect to the spin orbitals $\varphi_{i,f}(\mathbf{x})$, with the orbital energies $\varepsilon_{i,f}$. Furthermore, we use the fact that $\sum_{\{N_{el}\}} P_{\{N_{el}\}} n_i^{\{N_{el}\}}$ represents the average number of particles in the orbital φ_i and is thus denoted by \bar{n}_i . At zero temperature ($T = 0$), we have $\bar{n}_i = N_{n_i, l_i} / \{2(2l_i + 1)\}$, with N_{n_i, l_i} denoting the number of electrons in subshell (n_i, l_i) . Likewise, $\bar{n}_f = N_{n_f, l_f} / \{2(2l_f + 1)\}$.

For bound final states, N_{n_f, l_f} is the number of electrons in the final state characterized by the quantum numbers (n_f, l_f) .

In what follows we will apply Eq. (7) only to describe direct electron-impact ionization, i.e., a bound-to-free transition that ends up with the ejection of a bound electron into the continuum. We will not consider here the indirect excitation-autoionization channel—when an electron excitation is followed by a relaxation of the excited atom by ejecting an electron.

We proceed by implementing the ansatz from Eq. (3) for the spin orbitals $\varphi_{i,f}(\mathbf{x})$, which gives the following final expression for the DDCS,

$$\begin{aligned} \frac{d^2\sigma}{d\Omega_{\mathbf{q}_{\text{out}}} dE_{\text{out}}} &= \frac{4}{Q^4} \frac{q_{\text{out}}}{q_{\text{in}}} \sum_{n_f, l_f}^{\text{free}} \sum_{n_i, l_i}^{\text{occ.}} \delta(E_{\text{out}} - E_{\text{in}} - \varepsilon_{n_i, l_i} + \varepsilon_f) \\ &\times N_{n_i, l_i} \left[1 - \frac{N_{n_f, l_f}}{2(2l_f + 1)} \right] \sum_{L=0}^{l_i + l_f} (2L + 1) \\ &\times |R_{n_f, l_f, n_i, l_i}^L(Q) C_{l_i 0 L 0}^{l_f 0}|^2, \end{aligned} \quad (8)$$

where we explicitly denoted the orbital energy of the subshell (n_i, l_i) as ε_{n_i, l_i} , and where

$$R_{n_f, l_f, n_i, l_i}^L(Q) = \int_0^{R_{\text{max}}} dr u_{n_f l_f}(r) j_L(Qr) u_{n_i l_i}(r). \quad (9)$$

Here, $j_L(Qr)$ is a spherical Bessel function, and $C_{l_i 0 L 0}^{l_f 0}$ is a Clebsch-Gordan coefficient, which, due to the fact that $m_i = m_f = M = 0$, has the property that $l_i + l_f + L$ is an even integer in order to give a nonzero contribution. As we consider only ionization processes at zero temperature, we can set $N_{n_f, l_f} = 0$. Note that the sum $\sum_{n_f, l_f}^{\text{free}}$ only accounts for the situation when the ejected electron is free after the scattering process, i.e., when the system becomes ionized.

Let us consider the sum over the unoccupied final states. According to Eq. (8), these final states can be labeled with quantum numbers n_f and l_f . However, since we are considering bound-to-free transitions, the final states lie in the continuous part of the energy spectrum and cannot be labeled by the discrete number n_f . Instead, this label is replaced by the continuous parameter ε_f . The term $\sum_{n_f, l_f}^{\text{free}}$ should thus be read as $\sum_{l_f} \int d\varepsilon_f \rho_{l_f}(\varepsilon_f)$, where $\rho_{l_f}(\varepsilon_f)$ denotes the density of final states in between ε_f and $\varepsilon_f + d\varepsilon_f$, for a single discrete value of l_f . For energy-normalized wave functions $\rho_{l_f}(\varepsilon_f)$ reduces to unity, so we will omit it henceforth.

Conventionally, XATOM calculates the discrete bound states $u_{el}(r)$ and the continuous free states $u_{el}(r)$ in two different ways. The bound states are calculated with the generalized pseudospectral method on a nonuniform radial grid [54], whereas the free states are determined by numerically solving the radial Schrödinger equation for a given ε using a fourth-order Runge-Kutta method on a uniform grid [56]. However, due to the implementation of both a uniform and a nonuniform grid, transitions from initial bound states to final free states require an interpolation between the two grids. This interpolation has to occur for every ε in the wide range of the energy spectrum and is, therefore, computationally expensive. As we are exclusively interested in bound-to-free transitions for impact ionization, we overcome this difficulty by working

only with the nonuniform grid and by approximating free states with a discrete nonuniform continuum: a *pseudocontinuum*. The latter step will be discussed in detail in the next section.

C. Implementation of pseudocontinuum for DDCS calculation

Recall that the DDCS in the HFS framework of XATOM takes on the following form in Eq. (8):

$$\begin{aligned} & \frac{d^2\sigma}{d\Omega_{\mathbf{q}_{\text{out}}}dE_{\text{out}}} \\ &= \frac{4}{Q^4} \frac{q_{\text{out}}}{q_{\text{in}}} \sum_{n_i, l_i}^{\text{occ.}} \sum_{l_f} \int d\varepsilon_f \delta(\varepsilon_f - \varepsilon_{n_i, l_i} + E_{\text{out}} - E_{\text{in}}) \\ & \times N_{n_i, l_i} \sum_{L=0}^{l_i+l_f} (2L+1) |R_{\varepsilon_f, l_f, n_i, l_i}^L(Q) C_{l_i, 0L0}^{l_f 0}|^2 \\ & \equiv \frac{4}{Q^4} \frac{q_{\text{out}}}{q_{\text{in}}} \sum_{n_i, l_i}^{\text{occ.}} \sum_{l_f} \int d\varepsilon_f f_{\varepsilon_f, l_f}^{(n_i, l_i)} \delta(\varepsilon_f - \Delta E^{(n_i, l_i)}), \end{aligned} \quad (10)$$

where we have defined $\Delta E^{(n_i, l_i)} = E_{\text{in}} - E_{\text{out}} + \varepsilon_{n_i, l_i}$, and

$$f_{\varepsilon_f, l_f}^{(n_i, l_i)} = N_{n_i, l_i} \sum_{L=0}^{l_i+l_f} (2L+1) |R_{\varepsilon_f, l_f, n_i, l_i}^L(Q) C_{l_i, 0L0}^{l_f 0}|^2. \quad (11)$$

In order to calculate the DDCS, we need to evaluate ε_f and $f_{\varepsilon_f, l_f}^{(n_i, l_i)}$. As previously discussed, we calculate only discrete values of these quantities, which then define the pseudospectrum ε_{n_f} and $f_{n_f, l_f}^{(n_i, l_i)}$, with n_f denoting a discrete index, running from 1 to a certain finite integer number N . The question then arises as to how one can impose the proper energy normalization on the wave functions that comprise the obtained spectrum. To solve this issue, we assume that the calculated pseudospectrum is dense enough so that we can use local information on wave functions u_{n_f, l_f} and u_{n_f+1, l_f} , which have the corresponding energies ε_{n_f} and ε_{n_f+1} satisfying $\varepsilon_{n_f} \leq \varepsilon_f < \varepsilon_{n_f+1}$, similar to what was done in Refs. [57] and [58].

Our task is then to calculate an expression of the form $f_{l_f}^{(n_i, l_i)}(\Delta E^{(n_i, l_i)}) = \int d\varepsilon_f \delta(\varepsilon_f - \Delta E^{(n_i, l_i)}) f_{\varepsilon_f, l_f}^{(n_i, l_i)}$ by using a discrete pseudospectrum consisting of ε_{n_f} and $f_{n_f, l_f}^{(n_i, l_i)}$. Let us first integrate the function $f_{\varepsilon_f, l_f}^{(n_i, l_i)}$ up to a cutoff value $\Delta E^{(n_i, l_i)}$. The reason for this action will become apparent at the end of the explanation. Using our pseudospectrum, we can approximate this integral by the sum

$$\int^{\Delta E^{(n_i, l_i)}} d\varepsilon_f f_{\varepsilon_f, l_f}^{(n_i, l_i)} \approx \sum_{n_f=1}^m f_{n_f, l_f}^{(n_i, l_i)} \equiv \tilde{F}_{l_f}(\Delta E^{(n_i, l_i)}), \quad (12)$$

where $\varepsilon_m \leq \Delta E^{(n_i, l_i)} < \varepsilon_{m+1}$. $\tilde{F}_{l_f}(\Delta E^{(n_i, l_i)})$ is a histogram, where each value represents a partial, cumulative sum of $f_{n_f, l_f}^{(n_i, l_i)}$. The derivative of $\tilde{F}_{l_f}(\Delta E^{(n_i, l_i)})$ with respect to $\Delta E^{(n_i, l_i)}$, given by

$$\tilde{F}'_{l_f}(\Delta E^{(n_i, l_i)}) \equiv \sum_{n_f=1}^m f_{n_f, l_f}^{(n_i, l_i)} \delta(\varepsilon_{n_f} - \Delta E^{(n_i, l_i)}), \quad (13)$$

provides a discretized approximation of the quantity $f_{l_f}^{(n_i, l_i)}(\Delta E^{(n_i, l_i)}) = \int d\varepsilon_f \delta(\varepsilon_f - \Delta E^{(n_i, l_i)}) f_{\varepsilon_f, l_f}^{(n_i, l_i)}$. However,

$\tilde{F}'_{l_f}(\Delta E^{(n_i, l_i)})$ suffers from the same δ -singularity problem. In order to overcome this issue, we connect the neighboring midpoints of the histogram values of $\tilde{F}_{l_f}(\Delta E^{(n_i, l_i)})$, constructing a piecewise linear function $F_{l_f}(\Delta E^{(n_i, l_i)})$. The derivative of *this* function, $F'_{l_f}(\Delta E^{(n_i, l_i)})$, will be a histogram and contains no δ functions. It can be shown [57,58] that, with the increasing N , the function $F'_{l_f}(\Delta E^{(n_i, l_i)})$ converges to the correct value of $f_{l_f}^{(n_i, l_i)}(\Delta E^{(n_i, l_i)}) = \int d\varepsilon_f \delta(\varepsilon_f - \Delta E^{(n_i, l_i)}) f_{\varepsilon_f, l_f}^{(n_i, l_i)}$.

Using the method above, the DDCS is calculated by

$$\frac{d^2\sigma}{d\Omega_{\mathbf{q}_{\text{out}}}dE_{\text{out}}} = \frac{4}{Q^4} \frac{q_{\text{out}}}{q_{\text{in}}} \sum_{n_i, l_i}^{\text{occ.}} \sum_{l_f=0}^{l_{\text{max}}} \sum_{n_f=1}^m f_{n_f, l_f}^{(n_i, l_i)}, \quad (14)$$

where m is defined so as to uphold the relation $\varepsilon_m \leq \Delta E^{(n_i, l_i)} < \varepsilon_{m+1}$, and

$$f_{n_f, l_f}^{(n_i, l_i)} = N_{n_i, l_i} \sum_{L=0}^{l_i+l_f} (2L+1) |R_{\varepsilon_f, l_f, n_i, l_i}^L(Q) C_{l_i, 0L0}^{l_f 0}|^2. \quad (15)$$

With the calculated DDCS, we also have access to the singly differential cross sections, both angle- and energy-resolved, as well as to the total cross section (CS). In what follows we shall call the energy-resolved cross section DCS_E , whereas we define the DCS_θ to be the angle-resolved cross section, integrated over the azimuthal angle ϕ , i.e., $\text{DCS}_\theta = \int_0^{2\pi} d\phi (d\sigma/d\Omega_{\mathbf{q}_{\text{out}}})$. This integration can be immediately evaluated as the DDCS exhibits no dependence on ϕ . The upper limit of the energy integral, needed for the CS and DCS_θ , is chosen such that for each channel (n_i, l_i), only ionization is considered. These calculations that involve an energy integral can also be evaluated immediately due to the presence of the δ function, negating the need for the machinery outlined above. Otherwise, when an explicit integral evaluation is needed, we employ nonuniform Gaussian quadrature.

D. BEB and Lotz models

Here we provide a short description of the BEB [46] and Lotz [45] models, as they will be compared to our results in Sec. III. The binary-encounter-Bethe method [46] provides a simplified formula based on a binary collision theory for direct electron-impact ionization. The BEB cross section (σ_{BEB}) is orbital specific. It depends on the orbital binding energy B , the orbital kinetic energy U , the electron occupation number N , and the dipole constant Q . The BEB cross section for each orbital is given by the following expression [59]:

$$\begin{aligned} \sigma_{\text{BEB}} = & \frac{S}{t + (u+1)/n} \left[\frac{Q \ln t}{2} \left(1 - \frac{1}{t^2} \right) \right. \\ & \left. + (2 - Q) \left(1 - \frac{1}{t} - \frac{\ln t}{t+1} \right) \right], \end{aligned} \quad (16)$$

where T is the energy of the incoming electron, $t = T/B$, $u = U/B$, $S = 4\pi a_0^2 N (R/B)^2$, $a_0 = 0.52918 \text{ \AA}$, $R = 13.6057 \text{ eV}$, and n is the principal quantum number of the orbital. In an ad hoc fashion, n is set to be 1 if $n < 3$. The dipole constant Q is defined in terms of the continuum dipole oscillator strength and the kinetic energy of the ejected electron. In most cases, Q is set to be equal to 1. The total cross section is a sum of these orbital contributions.

For some neutral atoms and ground-state ions, the orbital parameter B , required for evaluating Eq. (16), is available in the NIST database [59]. However, for most elements, the experimental data required for the input of the BEB formula are scarce, and in the case of exotic core-hole configurations of ions, they are mostly absent. In the former case, it is advised to use theoretically computed values instead [59], and we adopted this to the latter case as well. Therefore, we use B and U , which is a purely theoretical quantity, as obtained from the Hartree-Fock-Slater calculation performed with XATOM. Note that this implementation of the BEB formula using XATOM-evaluated atomic parameters has been used in XMDYN simulations [26,60]. Note further that the BEB formula makes no mention of the wave functions of the electrons within the target. Any contribution arising from a transition matrix element is therefore not accounted for. An incoming electron will distinguish two different systems with the same number of bound electrons only through a difference in the parameters B and U . How well this captures the difference in impact ionization for two ions with the same charge but of different electronic configuration is unknown.

The semiempirical formula provided by Lotz [45] for the total electron-impact-ionization cross section takes the following form:

$$\sigma_{\text{Lotz}} = \sum_{i=1}^N a_i q_i \frac{\ln(E/P_i)}{E P_i} (1 - b_i \exp[-c_i(E/P_i - 1)]),$$

for $E \geq P_i$, (17)

where the sum over i runs over all N subshells, E is the energy of the incoming electron, P_i denotes the absolute value of the orbital energy of the i th subshell, and q_i is the equivalent number of electrons present per subshell. The constants a_i , b_i , and c_i are orbital specific. Their values are listed in Ref. [45]. For the exotic electronic configurations, we used orbital energy values obtained from XATOM calculations. We also note that a formula similar to Eq. (17), taking into account inner-shell excitations and autoionization, has been obtained in Ref. [61]. The Lotz formula in Eq. (17) is the result of a best-fit approximation using all single-electron impact-ionization cross-section data available at the time it was proposed [42–45]. As these data were obtained from ground-state ions and atoms, one cannot expect Eq. (17) to yield well-established results for ions with exotic electronic configurations.

We would like to emphasize that the use of the BEB and Lotz formulas for ions with exotic electronic configurations is not standard practice, as neither of them was designed to handle these cases. However, it is still done, in part, because both the BEB and Lotz formulas are computationally efficient. In Sec. III B, we test these formulas with exotic electronic configurations by comparing their predictions with our *ab initio* calculations.

III. RESULTS

Below we show electron-impact-ionization cross sections obtained for several electronic configurations of *carbon* and *sulfur* ions. These specific elements were selected due to their abundance in proteins and in biomolecules. In particular,

we considered C^+ , and C^{2+} ions with different electronic configurations: (i) with the hole(s) in the innermost shell ($1s^1 2s^2 2p^2$ and $1s^0 2s^2 2p^2$) and (ii) with the hole(s) in the outermost valence shell ($1s^2 2s^2 2p^1$ and $1s^2 2s^2 2p^0$). For the sulfur ion, we removed eight electrons in order to show that the difference in cross sections obtained for two different electronic configurations of the same net charge is amplified for higher charge states. We considered either all holes in inner shells, or in valence shells ($1s^0 2s^0 2p^2 3s^2 3p^4$ and $1s^2 2s^2 2p^4 3s^0 3p^0$).

A. Doubly and singly differential electron-impact-ionization cross section

In Fig. 1 we show a contour plot of the DDCS (Mb $eV^{-1} \text{deg}^{-1}$ in a logarithmic scale) of a double core-hole ($1s^{-2}$) C^{2+} ion colliding with a 1-keV electron. The x and y axes show the scattering angle and the outgoing energy of the scattered electron, respectively. On the left panel, the DCS_E is plotted after the numerical integration over θ . To obtain converged results, this angular integration requires 50 angular grid points. The DCS_θ is plotted on the bottom panel. For the scattering-angle-resolved cross section, we only show the range from 0° to 60° , as the DDCS is almost negligible for $\theta \geq 60^\circ$. For the outgoing energy, we show the range from 800 to 1000 eV, in which the cross section is the largest. In total, about 12 200 data points were calculated, which took ~ 31 min on one Intel Xeon E5-1620 CPU, corresponding on average to about 6.4 data points calculated per second. We note that DCS_θ calculations were much faster (~ 49 s for the whole range) because there was no need to numerically evaluate the energy integral. We used $N = 400$ for the number of radial grid points for all plots in Fig. 1. The DDCS plotted in Fig. 1 was multiplied by a factor of 2π , stemming from an integration over the azimuthal angle ϕ .

Figure 1 shows the presence of the ionization thresholds in the double core-hole C^{2+} ion, both in the DDCS and in the DCS_E (calculated to be at 50.7 and 56.5 eV for the $2p$ and $2s$ edge, respectively). The DDCS and DCS_θ reveal a high preference for low scattering angles, which is a consequence of the Coulomb factor $1/Q^4$ in Eq. (8).

B. Total electron-impact-ionization cross section

In this section, we consider the total electron-impact-ionization cross sections for C^+ , C^{2+} , and S^{8+} , and compare our *ab initio* calculations for the ground-state ions to the experimental predictions [62–65], as well as to the Lotz [45] and BEB models [46]. The experimental data in Ref. [62] were provided with error bars, shown as a shaded orange area in the following figures. Additionally, for the carbon ions, a more recent review [63] was available, providing an additional set of recommended data. Figure 2 shows the electron-impact-ionization cross section for C^+ : (a) when the hole is in the valence shell and (b) when it is in the core shell. Figure 2(a) shows that our *ab initio* calculation (XATOM) is comparable to the results obtained from the Lotz and BEB models. In comparison with the experimental data, our result follows the quantitative trend of the data adequately. Both the initial rise at low incoming energies and the later decrease

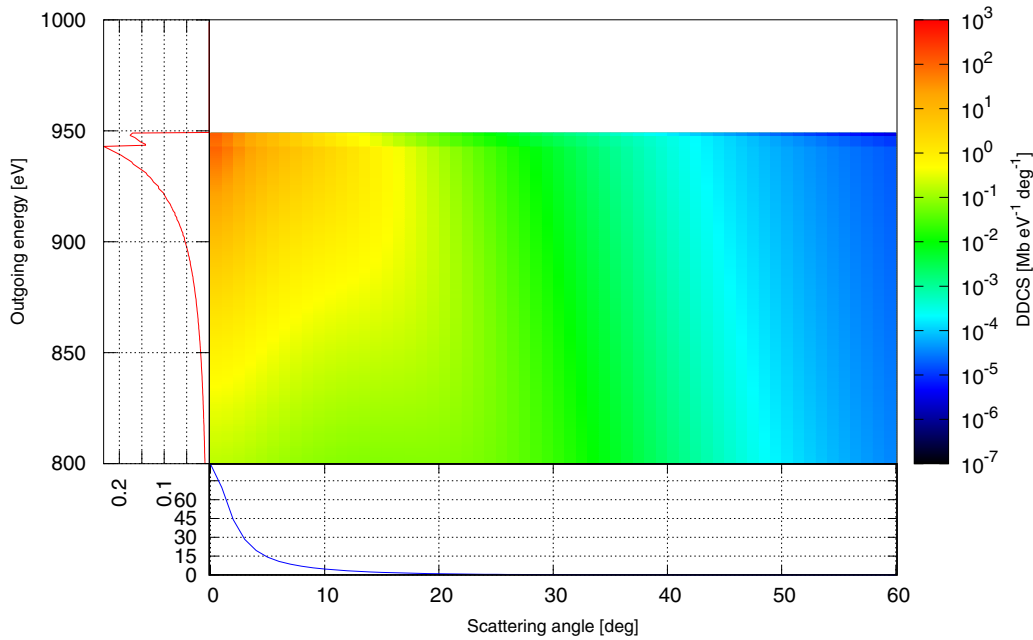


FIG. 1. A contour plot depicting the doubly differential electron-impact-ionization cross section [$\text{Mb eV}^{-1} \text{deg}^{-1}$] of a double core-hole C^{2+} ion, on a \log_{10} scale. The incident energy of the electron is 1 keV. The x axis shows the scattering angle θ from 0° to 60° , and the y axis shows the energy of the scattered electron E_{out} from 800 to 1000 eV. The DCS_θ is plotted in blue and has units of Mb deg^{-1} . The DCS_E is plotted in red and has units of Mb eV^{-1} . The white area on the top indicates the region of zero cross section below the $2p$ edge (50.7 eV).

at higher incoming energies are captured quite well by the XATOM result. Only in the intermediate region, where the peak is located, our result overestimates the cross section with respect to the experimental values before falling back into the proper range of values. Of course, improved results are expected for higher incoming electron energies due to the plane-wave formalism employed in the description of the incoming electron. Comparing with Fig. 2(b), we can observe that both Lotz and BEB results differ slightly for both the core-hole and the valence-hole cases, similarly as the XATOM results. The CPU runtime for a single total cross-section calculation

with XATOM is dependent on the incoming electron energy; it was 10.5 s on average.

Figure 3 shows the total electron-impact-ionization cross section for C^{2+} with (a) two valence holes and (b) two core holes. Figures 3(a) and 3(b) demonstrate that for higher ion charges the difference in cross sections calculated for the distinct electronic configurations becomes more pronounced. In particular, Fig. 3(a) shows a similar trend as in Fig. 2(a), where the XATOM result was comparable to both Lotz and BEB models. Also, the XATOM result shows a similar kind of relation with the experimental data: the initial rise and later decrease of

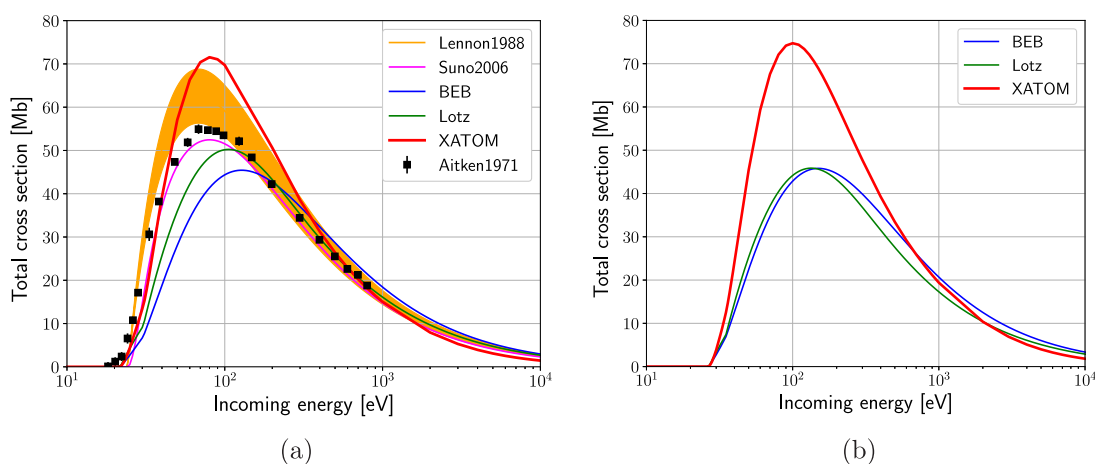


FIG. 2. Total electron-impact-ionization cross section as a function of incoming electron energy in eV for C^+ with (a) one valence hole ($2p^{-1}$) and (b) one core hole ($1s^{-1}$). The XATOM label denotes the present *ab initio* calculations, in comparison with the BEB method [46] and the Lotz method [45]. For the ground-state C^+ ion, the predictions are also compared with experimental data (Aitken *et al.*, 1971 [64], Lennon *et al.*, 1988 [62], and Suno and Kato, 2006 [63]).

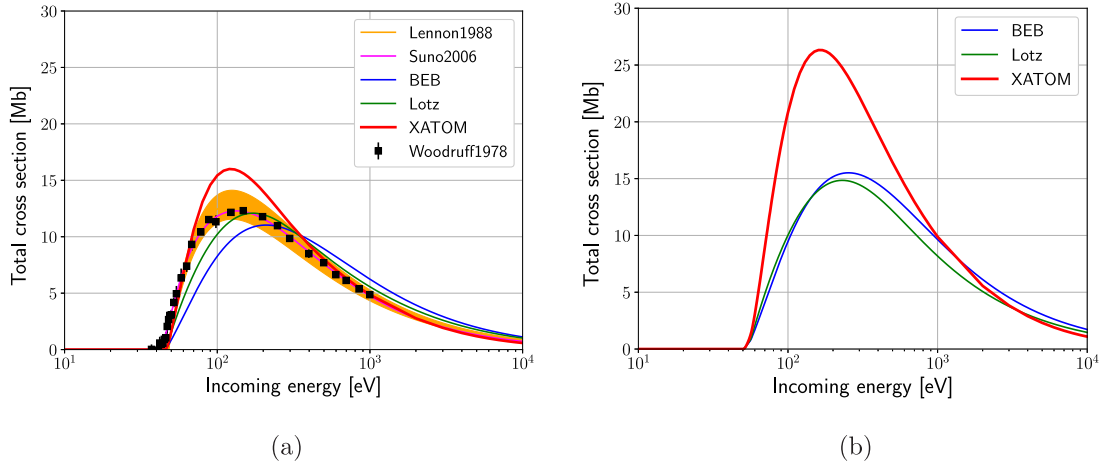


FIG. 3. Total electron-impact-ionization cross section as a function of incoming electron energy in eV for C²⁺ with (a) two valence holes (2p⁻²) and (b) two core holes (1s⁻²). For the ground-state configuration (a), three experimental data sets (Woodruff *et al.*, 1978 [65], Lennon *et al.*, 1988 [62], and Suno and Kato, 2006 [63]) are compared with theory predictions.

the data are reproduced quite accurately by XATOM, whereas it overestimates the values around the peak. Similarly, Fig. 3(b) again shows that both Lotz and BEB results differ slightly for the core-hole and the valence-hole cases. However, the XATOM result predicts a relatively large difference in cross sections for these cases.

Figure 4 shows the S⁸⁺ case: (a) with eight outer holes (2p⁻²3s⁻²3p⁻⁴) and (b) with eight inner holes (1s⁻²2s⁻²2p⁻⁴). For the ground-state configuration in Fig. 4(a), a trend similar to the carbon cases can be identified. By comparing Figs. 4(a) and 4(b), a large difference between total cross section for distinct electronic configurations becomes visible. We note that the positions of the maximum of the total cross section predicted with XATOM resemble the experimental ones more closely than those predicted with the Lotz and BEB models for all three cases considered. We have restricted the incoming electron energy to a maximum of 10 keV. At higher electron energies, relativistic effects [47,48] become increasingly important. These are currently not incorporated in our approach.

We conclude this section with an error estimate of our approach. As mentioned in Sec. II B, the incoming electron is described in a plane-wave formalism, which is an increasingly accurate description for higher incoming electron energies. Therefore, we will perform our error estimate as follows: We choose two values of the incoming energy, one for the representation of low incoming energies and the other for high energies. We chose 100 eV and 1 keV, respectively, for C⁺ and C²⁺, whereas for S⁸⁺ we chose 1 and 10 keV for the low and high incoming energy regime, respectively. At these points, we compare the values of the impact-ionization cross section for the ground-state ions between XATOM and the experimental dataset of Lennon *et al.* [62] in order to obtain an upper limit for the percentage error estimate for the XATOM result. We chose this dataset to have a consistent comparison for all systems. At 100 eV, the error estimates for C⁺ and C²⁺ are 18% and 24%, respectively, whereas at 1 keV they are 6.2% and 1.2%, respectively. The error estimates for S⁸⁺ are 25% at 1 keV and 14% at 10 keV. We argue that, since XATOM treats ground-state ions and exotic ions within a consistent *ab initio* framework,

we expect at most the same percentage errors for the core-hole ions as for the ground-state ones.

C. Discussion

Below we discuss the observed trends in impact-ionization cross sections when comparing ground-state ions to their core-hole variants. Figures 2, 3, and 4 show that the impact-ionization cross section calculated by XATOM is larger for the core-hole configurations than for the ground-state ions. The magnitude of the difference depends on both the ion charge and the energy of the incoming electron. The Lotz result does not follow this trend generally. As observed in Figs. 2(a) and 2(b), the Lotz result shows that the core-hole ion has a smaller cross section than the ground-state ion. We attribute this to the inapplicability of the Lotz formula for ions with exotic electronic configurations, as already discussed in Sec. II D. On the other hand, the BEB result does follow the trend of the XATOM result in all cases considered, albeit to a smaller extent. We argue that the physical reason behind this trend is a combination of two mutually competing factors in the core-hole ions. On the one hand, there are more valence electrons to interact with, which increases the cross sections. On the other hand, this effect is partly compensated by the change in orbital size due to the increased positive charge seen by valence electrons and results in a slight decrease of the cross sections. We will first make our arguments for the XATOM calculations, after which we will show why the BEB result follows the same trend.

The contribution to the total impact-ionization cross section from core-shell electrons calculated by XATOM was observed to be very small as compared to the contribution from valence-shell electrons, which is consistent with previous works [46]. For the purposes of this discussion, the contribution of core shells can be neglected. Now consider the example of C²⁺. The ground-state ion has two electrons left in the 2s valence shell. In contrast, its double core-hole variant has four valence electrons which will contribute to the impact-ionization cross section, and so we would expect to see the cross section for the double core-hole case to be approximately double the one for the ground-state ion. This is indeed the case for incoming

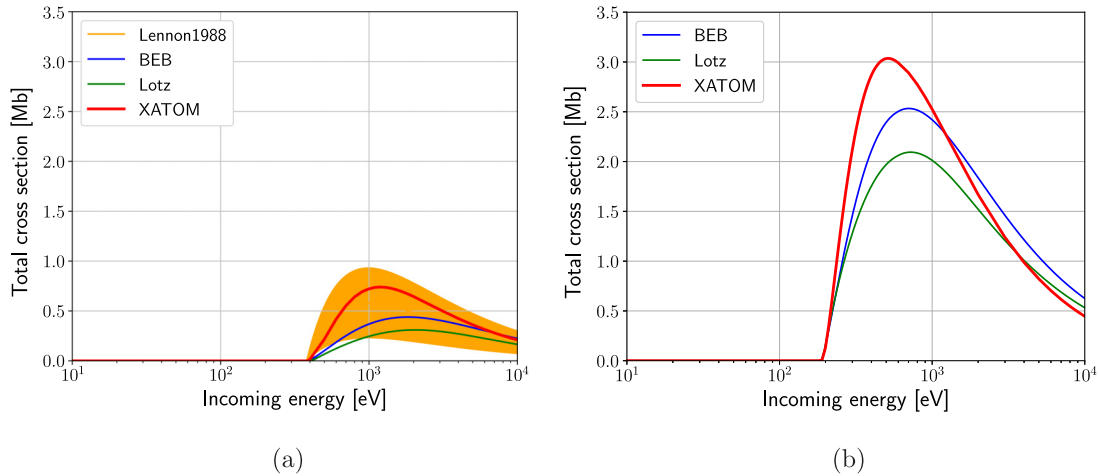


FIG. 4. Total electron-impact-ionization cross section as a function of incoming electron energy in eV for S^{8+} with (a) eight outer holes ($2p^{-2}3s^{-2}3p^{-4}$) and (b) eight inner holes ($1s^{-2}2s^{-2}2p^{-4}$). For the ground-state configuration (a), the experimental data set from [62] is shown.

energies above 1 keV, as shown in Fig. 3. A similar conclusion can be drawn for C^+ , only now the cross section for the single valence-hole and single core-hole ions should not differ by a factor of 2 but by a factor of 4/3, since we move from a case with three valence electrons to one with four. This is again observed in Fig. 2 for the energies beyond 1 keV. As for S^{8+} , the eight-core-hole ion has six more valence electrons than its eight-valence-hole variant. The cross sections for the two S^{8+} variants never differ by as much as a factor of 6 for the incoming energies considered, as is seen in Fig. 4. Instead, a factor of 3.5 can be deduced at most.

This leaves us to find some features of the core-hole variants of S^{8+} , C^{2+} , and C^+ , which compensate the effect of the increase in cross section due to the presence of more valence electrons, and which manifest themselves more for lower energies in the case of the carbon ions. To this end, note that the argument based on counting valence electrons assumes that the contributions to the cross section of the valence shells in the core-hole variants are roughly the same. However, for both C^+ and C^{2+} , we observed that the contribution from the 2s shell is smaller for the core-hole ion variant as compared to the ground-state ion, the difference of which diminishes for higher incoming energies. Since the configurations of S^{8+} we considered have no orbitals which contain the same amount of electrons, such a comparison is less meaningful for S^{8+} . We attribute this to the decreased size of the valence orbitals in the core-hole variants caused by the increased positive charge they experience from the nucleus, as there is no screening effect from core electrons. To understand why a smaller orbital leads to a diminished contribution in the cross section, let us consider the transition matrix element in the expression for the impact-ionization cross section in Eq. (7). Also, we will separately consider low incoming energies (of the order of 100 eV) and high ones (1 keV or higher) in what follows.

Let us start with the regime of low incoming electron energies (take $E_{in} = 100$ eV) and consider the matrix element $\langle \varphi_f | e^{i\mathbf{Q}\cdot\mathbf{x}} | \varphi_i \rangle$. For an electron of 100 eV, the de Broglie wavelength is of the order of 1 Å. Since the ejected electron energy is less than the incoming electron energy, the de Broglie

wavelength of the ejected electron will be larger than 1 Å. However, this is much larger than the spatial extent of the initial orbitals we are considering. Therefore, when performing the integration of $\langle \varphi_f | e^{i\mathbf{Q}\cdot\mathbf{x}} | \varphi_i \rangle$, we can largely consider $\langle \varphi_f |$ to be a constant. What remains is an integration over $e^{i\mathbf{Q}\cdot\mathbf{x}} \varphi_i(\mathbf{x})$, which is simply the Fourier component of the initial orbital associated with \mathbf{Q} , denoting the momentum transfer from the incoming electron. Effectively, we are considering the momentum distribution of the initial orbital $|\varphi_i\rangle$, evaluated at the momentum transfer \mathbf{Q} . However, not all values of \mathbf{Q} are considered. Since $\mathbf{Q} = \mathbf{q}_{in} - \mathbf{q}_{out}$, and, for our incoming electron, \mathbf{q}_{in} is of the order of $\sqrt{2E_{in}}$, \mathbf{Q} will not sample many points in the momentum distribution of $|\varphi_i\rangle$ for low energies. Combining this with the fact that smaller initial orbitals will have a more spread out momentum distribution leads to a smaller transition matrix element, thus diminishing the contribution to the impact-ionization cross section.

At higher energies (for example, $E_{in} = 1$ keV), the energy transfer from the incoming electron may be substantial, so we cannot assume the de Broglie wavelength of the ejected electron to be constant when performing integration of the matrix element $\langle \varphi_f | e^{i\mathbf{Q}\cdot\mathbf{x}} | \varphi_i \rangle$. However, in such cases, \mathbf{Q} will include a much larger range of values to sample over. Additionally, we can argue that the highly energetic ejected electron could equally well be described as a plane wave with an associated momentum \mathbf{q}_{eject} . Then the transition matrix element will be an integral over $e^{i(\mathbf{Q}-\mathbf{q}_{eject})\cdot\mathbf{x}} \varphi_i(\mathbf{x})$. From here on, we can reuse the Fourier analysis argument from the low-energy case. Again, a smaller initial orbital will lead to a spread in its momentum distribution, but since \mathbf{Q} will include a much larger range of values for sampling, we can argue that the diminishing effect to the cross-section contribution will be less present for higher energies. This last effect is not seen in the S^{8+} case, because the much stronger Coulomb interaction experienced by the incoming electron, as compared to the C^+ and C^{2+} cases, pushes the validity of the plane-wave framework to higher energies than those that were considered.

These two factors which we have discussed above are also captured, to a different extent, by the BEB formula. First,

TABLE I. The orbital kinetic energies in [eV] as calculated by XATOM for all systems considered and used for the calculation of the BEB cross sections.

	Orbital kinetic energies U [eV]				
	$1s$	$2s$	$2p$	$3s$	$3p$
$C^+ (1s^{-1})$	478.9	67.6	63.8	-	-
$C^+ (2p^{-1})$	447.0	54.1	45.5	-	-
$C^{2+} (1s^{-2})$	495.8	89.6	91.0	-	-
$C^{2+} (2p^{-2})$	448.6	60.9	54.1	-	-
$S^{8+} (1s^{-2} 2s^{-2} 2p^{-4})$	3469.5	801.1	810.5	271.5	268.6
$S^{8+} (2p^{-2} 3s^{-2} 3p^{-4})$	3332.4	582.7	567.1	179.9	169.3

the overall factor of N , denoting the number of electrons present in the orbital considered, is contained in Eq. (16). Second, the diminishing factor from the decreased orbital size is captured by the orbital kinetic energy U in the denominator of Eq. (16). We can relate the size of an orbital to the orbital kinetic energy as follows. The orbital kinetic energy is related to the momentum distribution of the target electron through $U = \langle \hat{p}^2 \rangle / 2$, with \hat{p} the momentum operator of an electron in a certain subshell. This means U is associated to the second moment of the momentum distribution, i.e., its width. As an orbital becomes smaller and thus more localized, its momentum distribution will spread, causing U to become larger and therefore decreasing the BEB cross section. In order to justify the observed trend in Figs. 2 and 3, this would imply that the orbital kinetic energies U of the core-hole variants should be larger than those of the ground-state ions. Table I shows the values of U for each shell of each system considered, as calculated by XATOM. It shows, without exception, that the orbital kinetic energies U of the core-hole variants are indeed larger than those of the ground-state ions. Therefore, the qualitative behavior of the BEB result follows that of our *ab initio* calculations.

IV. CONCLUSION AND OUTLOOK

To sum up, we have developed a versatile *ab initio* scheme for calculation of direct electron-impact ionization of ions in any electronic configuration at zero temperature within the Hartree-Fock-Slater (HFS) framework. In particular, we have incorporated the known formula for the doubly differential electron-impact-ionization cross section (DDCS) derived in Ref. [55] into the HFS-based XATOM toolkit. Within the scheme, the incoming electron and the scattered electron are treated using plane waves, the atomic system under consideration with a HFS approach, and the final state of the ejected electron with a pseudocontinuum description. From the DDCS obtained, we have calculated singly differential cross sections, both angle and energy resolved, as well as the total electron-impact-ionization cross section.

Our approach, derived in the first Born approximation, should work accurately not only for the description of electron-impact ionization of cold ions, but also for more complex systems like molecules, solids, and plasmas, provided that the

assumption of a weak scattering potential seen by the impact electron is reliable, i.e., the average interaction energy between the impact electron and the scatterer(s) is much lower than the kinetic energy of the impact electron. Following this criterion, we expect that especially in the condensed-matter systems, where the screening of ions diminishes the effect of long-range Coulomb interaction between the incoming electron and constituent ions, also the regime of lower electron-impact energies will be accessible for the impact-ionization cross sections calculated with this method.

The *ab initio* calculations can be easily incorporated in x-ray-induced dynamics simulations treating the relaxation of atoms after high-energy-impact collision and provide impact-ionization cross sections for any exotic (multihole) configuration.

On the examples of ground-state carbon and sulfur ions, we have shown that the results of our *ab initio* scheme for total electron-impact-ionization cross section manage to reproduce the experimental data at high energies of the incoming electron to a satisfactory degree, while resembling the overall trend of the data sets for all incoming energies considered. For the exotic configurations, for which no experimental data are available, our *ab initio* method enables us to perform cross-section calculations without any difficulties. Our results indicate that there are significant differences in impact-ionization cross sections between the core-hole (exotic) and valence-hole (ground-state) configurations in ions of the same charge, which increase with an increasing charge of the ions. Also, our results are, in general, comparable to those obtained with the BEB and Lotz models for core-hole configurations, using the input parameters calculated with XATOM. However, our method indicates stronger differences between the impact-ionization cross sections for core- and valence-hole configurations than the BEB and Lotz models. The discrepancies observed increase with increasing charge of the ions.

We expect that this finding can have a significant impact on any quantitative modeling studies treating the relaxation of atoms after high-energy-impact collision, e.g., simulations for coherent x-ray diffraction imaging of nanocrystals and single biological macromolecules, or studies of laser-created plasmas. While we advocate the use of an *ab initio* method, the need for repeated cross-section calculations in simulations of x-ray-driven complex systems requires striking a balance between numerical accuracy and computational efficiency. We believe that our implementation within XATOM satisfies these requirements. For quantitative checks, further studies are required in specific contexts. In particular, for dense samples, the inclusion of finite temperature and treatment of the ion's environment are necessary. This development is already underway.

ACKNOWLEDGMENTS

We would like to thank Zoltan Jurek and Malik Muhammad Abdullah for useful discussions, as well as Otfried Geffert for his aid in software development. These authors funding source is Deutsches Elektronen-Synchrotron (DESY).

[1] P. Emma, R. Akre, J. Arthur, R. Bionta, C. Bostedt, J. Bozek, A. Brachmann, P. Bucksbaum, R. Coffee, F.-J. Decker *et al.*, First

lasing and operation of an ångstrom-wavelength free-electron laser, *Nat. Photonics* **4**, 641 (2010).

- [2] T. Ishikawa, H. Aoyagi, T. Asaka, Y. Asano, N. Azumi, T. Bizen, H. Ego, K. Fukami, T. Fukui, Y. Furukawa *et al.*, A compact x-ray free-electron laser emitting in the sub-ångström region, *Nat. Photonics* **6**, 540 (2012).
- [3] T. Tschentscher, C. Bressler, J. Grünert, A. Madsen, A. P. Mancuso, M. Meyer, A. Scherz, H. Sinn, and U. Zastra, Photon beam transport and scientific instruments at the European XFEL, *Appl. Sci.* **7**, 592 (2017).
- [4] H.-S. Kang, C.-K. Min, H. Heo, C. Kim, H. Yang, G. Kim, I. Nam, S. Y. Baek, H.-J. Choi, G. Mun *et al.*, Hard x-ray free-electron laser with femtosecond-scale timing jitter, *Nat. Photonics* **11**, 708 (2017).
- [5] C. J. Milne, T. Schietinger, M. Aiba, A. Alarcon, J. Alex, A. Anghel, V. Arsov, C. Beard, P. Beaud, S. Bettoni *et al.*, SwissFEL: The Swiss x-ray free electron laser, *Appl. Sci.* **7**, 720 (2017).
- [6] L. Young, E. P. Kanter, B. Krässig, Y. Li, A. M. March, S. T. Pratt, R. Santra, S. H. Southworth, N. Rohringer, L. F. DiMauro *et al.*, Femtosecond electronic response of atoms to ultra-intense x-rays, *Nature (London)* **466**, 56 (2010).
- [7] M. Hoener, L. Fang, O. Kornilov, O. Gessner, S. T. Pratt, M. Guhr, E. P. Kanter, C. Blaga, C. Bostedt, J. D. Bozek *et al.*, Ultraintense X-Ray Induced Ionization, Dissociation, and Frustrated Absorption in Molecular Nitrogen, *Phys. Rev. Lett.* **104**, 253002 (2010).
- [8] B. Rudek, S.-K. Son, L. Foucar, S. W. Epp, B. Erk, R. Hartmann, M. Adolph, R. Andritschke, A. Aquila, N. Berrah *et al.*, Ultra-efficient ionization of heavy atoms by intense x-ray free-electron laser pulses, *Nat. Photonics* **6**, 858 (2012).
- [9] A. Rudenko, L. Inhester, K. Hanasaki, X. Li, S. J. Robotjazi, B. Erk, R. Boll, K. Toyota, Y. Hao, O. Vendrell *et al.*, Femtosecond response of polyatomic molecules to ultra-intense hard x-rays, *Nature (London)* **546**, 129 (2017).
- [10] S. Bernitt, G. V. Brown, J. K. Rudolph, R. Steinbrügge, A. Graf, M. Leutenegger, S. W. Epp, S. Eberle, K. Kubicek, V. Mäckel *et al.*, An unexpectedly low oscillator strength as the origin of the Fe XVII emission problem, *Nature (London)* **492**, 225 (2012).
- [11] S. M. Vinko, O. Ciricosta, B. I. Cho, K. Engelhorn, H.-K. Chung, C. R. D. Brown, T. Burian, J. Chalupský, R. W. Falcone, and C. Graves *et al.*, Creation and diagnosis of a solid-density plasma with an x-ray free-electron laser, *Nature (London)* **482**, 59 (2012).
- [12] R. Neutze, R. Wouts, D. van der Spoel, E. Weckert, and J. Hajdu, Potential for biomolecular imaging with femtosecond x-ray pulses, *Nature (London)* **406**, 752 (2000).
- [13] H. N. Chapman, P. Fromme, A. Barty, T. A. White, R. A. Kirian, A. Aquila, M. S. Hunter, J. Schulz, D. P. DePonte, U. Weierstall *et al.*, Femtosecond x-ray protein nanocrystallography, *Nature (London)* **470**, 73 (2011).
- [14] M. M. Seibert, T. Ekeberg, F. R. N. C. Maia, M. Svenda, J. Andreasson, O. Jónsson, D. Odić, B. Iwan, A. Rocker, D. Westphal *et al.*, Single mimivirus particles intercepted and imaged with an x-ray laser, *Nature (London)* **470**, 78 (2011).
- [15] S. Boutet, L. Lomb, G. J. Williams, T. R. M. Barends, A. Aquila, R. B. Doak, U. Weierstall, D. P. DePonte, J. Steinbrener, and R. L. Shoeman *et al.*, High-resolution protein structure determination by serial femtosecond crystallography, *Science* **337**, 362 (2012).
- [16] L. Redecke, K. Nass, D. P. DePonte, T. A. White, D. Rehders, A. Barty, F. Stellato, M. Liang, T. R. M. Barends, and S. Boutet *et al.*, Natively inhibited *Trypanosoma brucei* cathepsin B structure determined by using an x-ray laser, *Science* **339**, 227 (2013).
- [17] B. D. Patterson, Crystallography using an x-ray free-electron laser, *Crystallogr. Rev.* **20**, 242 (2014).
- [18] I. Schlichting, Serial femtosecond crystallography: The first five years, *IUCrJ* **2**, 246 (2015).
- [19] B. Rupp, *Biomolecular Crystallography: Principles, Practice, and Application to Structural Biology* (Garland Science, New York, 2009).
- [20] B. Ziaja, Z. Jurek, N. Medvedev, V. Saxena, S.-K. Son, and R. Santra, Towards realistic simulations of macromolecules irradiated under the conditions of coherent diffraction imaging with an x-ray free-electron laser, *Photonics* **2**, 256 (2015).
- [21] H. M. Quiney and K. A. Nugent, Biomolecular imaging and electronic damage using x-ray free-electron lasers, *Nat. Phys.* **7**, 142 (2011).
- [22] B. Ziaja, H. N. Chapman, R. Fäustlin, S. Hau-Riege, Z. Jurek, A. V. Martin, S. Toleikis, F. Wang, E. Weckert, and R. Santra, Limitations of coherent diffractive imaging of single objects due to their damage by intense x-ray radiation, *New J. Phys.* **14**, 115015 (2012).
- [23] U. Lorenz, N. M. Kabachnik, E. Weckert, and I. A. Vartanyants, Impact of ultrafast electronic damage in single-particle x-ray imaging experiment, *Phys. Rev. E* **86**, 051911 (2012).
- [24] M. M. Abdullah, Z. Jurek, S.-K. Son, and R. Santra, Calculation of x-ray scattering patterns from nanocrystals at high x-ray intensity, *Struct. Dyn.* **3**, 054101 (2016).
- [25] S.-K. Son, L. Young, and R. Santra, Impact of hollow-atom formation on coherent x-ray scattering at high intensity, *Phys. Rev. A* **83**, 033402 (2011).
- [26] Z. Jurek, S.-K. Son, B. Ziaja, and R. Santra, XMDYN and XATOM: Versatile simulation tools for quantitative modeling of x-ray free-electron laser induced dynamics of matter, *J. Appl. Crystallogr.* **49**, 1048 (2016).
- [27] B. F. Murphy, T. Osipov, Z. Jurek, L. Fang, S.-K. Son, M. Mücke, J. H. D. Eland, V. Zhaunerchyk, R. Feifel, L. Avaldi *et al.*, Femtosecond x-ray-induced explosion of C_{60} at extreme intensity, *Nat. Commun.* **5**, 4281 (2014).
- [28] T. Tachibana, Z. Jurek, H. Fukuzawa, K. Motomura, K. Nagaya, S. Wada, P. Johnsson, M. Siano, S. Mondal, Y. Ito *et al.*, Nanoplasma formation by high intensity hard x-rays, *Sci. Rep.* **5**, 10977 (2015).
- [29] M. M. Abdullah, A. Z. Jurek, S. K. Son, and R. Santra, Molecular-dynamics approach for studying the nonequilibrium behavior of x-ray-heated solid-density matter, *Phys. Rev. E* **96**, 023205 (2017).
- [30] C. H. Yoon, M. V. Yurkov, E. A. Schneidmiller, L. Samoylova, A. Buzmakov, Z. Jurek, B. Ziaja, R. Santra, N. D. Loh, T. Tschentscher *et al.*, A comprehensive simulation framework for imaging single particles and biomolecules at the European x-ray free-electron laser, *Sci. Rep.* **6**, 24791 (2016).
- [31] R. Santra, Concepts in x-ray physics, *J. Phys. B* **42**, 023001 (2009).
- [32] H. N. Chapman, C. Caleman, and N. Timneanu, Diffraction before destruction, *Philos. Trans. R. Soc. B* **369**, 20130313 (2014).
- [33] R. Henderson, Cryo-protection of protein crystals against radiation damage in electron and x-ray diffraction, *Proc. R. Soc. London B* **241**, 6 (1990).

- [34] R. F. Egerton, Control of radiation damage in the TEM, *Ultramicroscopy* **127**, 100 (2013).
- [35] S. M. Vinko, O. Ciricosta, T. R. Preston, D. S. Rackstraw, C. R. D. Brown, T. Burian, J. Chalupský, B. I. Cho, H.-K. Chung, K. Engelhorn *et al.*, Investigation of femtosecond collisional ionization rates in a solid-density aluminium plasma, *Nat. Commun.* **6**, 6397 (2015).
- [36] I.-J. Kang and W. D. Foland, Theory of electron impact excitation and ionization of atoms and ions, *Phys. Rev.* **164**, 122 (1967).
- [37] M. R. H. Rudge, Theory of the ionization of atoms by electron impact, *Rev. Mod. Phys.* **40**, 564 (1968).
- [38] P. L. Bartlett and A. T. Stelbovics, Calculation of electron-impact total-ionization cross sections, *Phys. Rev. A* **66**, 012707 (2002).
- [39] J. Berakdara, A. Lahmam-Bennani, and C. D. Cappello, The electron-impact double ionization of atoms: An insight into the four-body Coulomb scattering dynamics, *Phys. Rep.* **374**, 91 (2003).
- [40] O. Al-Hagan, *Theoretical Study of Electron Impact-ionization of Molecules*, Doctoral Dissertation (Missouri University of Science and Technology, Rolla Missouri, 2010).
- [41] H. Ehrhardt, K. Jung, G. Knoth, and P. Schlemmer, Differential cross sections of direct single electron impact ionization, *Z. Phys. D* **1**, 3 (1985).
- [42] W. Lotz, Ionization potentials of atoms and ions from hydrogen to zinc, *J. Opt. Soc. Am.* **57**, 873 (1967).
- [43] W. Lotz, An empirical formula for the electron-impact ionization cross-section, *Z. Phys.* **206**, 205 (1967).
- [44] W. Lotz, Electron-impact ionization cross-sections and ionization rate coefficients for atoms and ions from hydrogen to calcium, *Z. Phys.* **216**, 241 (1968).
- [45] W. Lotz, Electron-impact ionization cross-sections for atoms up to $Z = 108$, *Z. Phys.* **232**, 101 (1970).
- [46] Y.-K. Kim and M. E. Rudd, Binary-encounter-dipole model for electron-impact ionization, *Phys. Rev. A* **50**, 3954 (1994).
- [47] Y.-K. Kim, J. P. Santos, and F. Parente, Extension of the binary-encounter-dipole model to relativistic incident electrons, *Phys. Rev. A* **62**, 052710 (2000).
- [48] M. Guerra, F. Parente, P. Indelicato, and J. P. Santo, Modified binary encounter Bethe model for electron-impact ionization, *Int. J. Mass Spectrom.* **313**, 1 (2012).
- [49] S.-K. Son, J. J. Bekx, K. Toyota, O. Geffert, J. M. Slowik, and R. Santra, *XATOM—An Integrated Toolkit for X-Ray and Atomic Physics*, CFEL, DESY, rev. 2885 (Hamburg, Germany, 2017).
- [50] J. M. Slowik, S.-K. Son, G. Dixit, Z. Jurek, and R. Santra, Incoherent x-ray scattering in single molecule imaging, *New J. Phys.* **16**, 073042 (2014).
- [51] S.-K. Son, O. Geffert, and R. Santra, Compton spectra of atoms at high x-ray intensity, *J. Phys. B* **50**, 064003 (2017).
- [52] J. C. Slater, A simplification of the Hartree-Fock method, *Phys. Rev.* **81**, 385 (1951).
- [53] R. Latter, Atomic energy levels for the Thomas-Fermi and Thomas-Fermi-Dirac potential, *Phys. Rev.* **99**, 510 (1955).
- [54] G. Yao and S. I. Chu, Generalized pseudospectral methods with mappings for bound and resonance state problems, *Chem. Phys. Lett.* **204**, 381 (1993).
- [55] K. Sturm, Dynamic structure factor: An introduction, *Z. Naturforsch. A* **48**, 233 (1993).
- [56] J. W. Cooper, Photoionization from outer atomic subshells, A model study, *Phys. Rev.* **128**, 681 (1962).
- [57] R. Santra and L. S. Cederbaum, Non-Hermitian electronic theory and applications to clusters, *Phys. Rep.* **368**, 1 (2002).
- [58] P. W. Langhoff, in *Electron-Molecule and Photon-Molecule Collisions*, edited by T. Rescigno, V. McKoy, and B. Schneider (Plenum Press, New York, 1979).
- [59] Available at <https://physics.nist.gov/PhysRefData/Ionization/intro.html>.
- [60] Z. Jurek, G. Faigel, and M. Tegze, Dynamics in a cluster under the influence of intense femtosecond hard x-ray pulses, *Eur. Phys. J. D* **29**, 217 (2004).
- [61] A. Burgess and M. C. Chidichimo, Electron impact ionization of complex ions, *Mon. Not. R. Astron. Soc.* **203**, 1269 (1983).
- [62] M. A. Lennon, K. L. Bell, H. B. Gilbody, J. G. Hughes, A. E. Kingston, M. J. Murray, and F. J. Smith, Recommended data on the electron impact ionization of atoms and ions: Fluorine to Nickel, *J. Phys. Chem. Ref. Data* **17**, 1285 (1988).
- [63] H. Suno and T. Kato, Cross section database for carbon atoms and ions: Electron-impact ionization, excitation, and charge exchange in collisions with hydrogen atoms, *At. Data Nucl. Data Tables* **92**, 407 (2006).
- [64] K. L. Aitken, M. F. A. Harrison, and R. D. Rundel, Measurement of the cross section for electron impact ionization of multi-electron ions, II. N^{2+} to N^{3+} and C^+ to C^{2+} , *J. Phys. B* **4**, 1189 (1971).
- [65] P. R. Woodruff, M.-C. Hublet, M. F. A. Harrison, and E. Brook, A measurement of the cross section for electron impact ionisation of C^{2+} , *J. Phys. B* **11**, L679 (1978).